Taylor & Francis
Taylor & Francis Group

Self-similarity and flow characteristics of vertical-axis wind turbine wakes: an LES study

Mahdi Abkar and John O. Dabiri

Center for Turbulence Research, Stanford University, Stanford, CA, USA

ABSTRACT

Large eddy simulation (LES) is coupled with a turbine model to study the structure of the wake behind a vertical-axis wind turbine (VAWT). In the simulations, a tuning-free anisotropic minimum dissipation model is used to parameterise the subfilter stress tensor, while the turbine-induced forces are modelled with an actuator line technique. The LES framework is first validated in the simulation of the wake behind a model straight-bladed VAWT placed in the water channel and then used to study the wake structure downwind of a full-scale VAWT sited in the atmospheric boundary layer. In particular, the self-similarity of the wake is examined, and it is found that the wake velocity deficit can be well characterised by a two-dimensional multivariate Gaussian distribution. By assuming a self-similar Gaussian distribution of the velocity deficit, and applying mass and momentum conservation, an analytical model is developed and tested to predict the maximum velocity deficit downwind of the turbine. Also, a simple parameterisation of VAWTs for LES with very coarse grid resolutions is proposed, in which the turbine is modelled as a rectangular porous plate with the same thrust coefficient. The simulation results show that, after some downwind distance ($x/D \approx 6$), both actuator line and rectangular porous plate models have similar predictions for the mean velocity deficit. These results are of particular importance in simulations of large wind farms where, due to the coarse spatial resolution, the flow around individual VAWTs is not resolved.

1. Introduction

Vertical-axis wind turbines (VAWTs) have attracted renewed attention in recent years due to their potential to fill important riches in renewable energy [1–7]. For instance, VAWTs are insensitive to the wind direction and hence do not require any yaw mechanism, and their drive train system is placed close to the ground [8]. It is also shown that VAWTs can potentially provide higher power output per unit land area than horizontal-axis wind turbines (HAWTs) [1]. This is mainly due in part to the fact that, unlike for HAWTs, the swept area of a VAWT can increase, independent of its footprint [9]. However, to date, VAWTs have not benefitted from as much research and development as HAWTs [8]. For this reason, there are fewer studies that investigate the structure and characteristics of VAWT wakes compared to HAWTs.

Brochier et al. [10] conducted one of the first experimental studies on the wake flow downwind of a VAWT. They studied the flow field downwind of a model straight-bladed VAWT through laser Doppler velocimeter (LDV) tests in a water channel. In particular, they focused on the tip-speed ratios (the ratio between the speed of the blades and the speed of the incoming flow), λ_R, at which the dynamic stall occurs. Bergeles et al. [11] carried out wind tunnel experiments using hot wire in the near-wake region of a Darrieus-type wind turbine. They reported the mean velocity and turbulence level profiles at two downstream positions ($x/D = 0.55$ and 1, where D is the rotor diameter) for different tip-speed ratios ($\lambda_R = 4.06$, 5.4 and 7.1). They showed that downstream of the turbine, the wake turns slightly towards the direction of rotation, with a maximum angle of deflection of 7° at the optimum tip-speed ratio ($\lambda_R = 4.06$). They also showed that the turbulence level is larger near the edges of the wake, where the mean wind shear is stronger, compared to the centre of the wake. Recently, Battisti et al. [12] performed wind tunnel measurements on the wake of a VAWT. They reported the mean velocity and turbulence intensity at one downstream position ($x/D = 1.5$) for two different tip-speed ratios ($\lambda_R = 1.6$ and 2.5). They showed that the wake appears to be asymmetric and deflected according to the rotational direction of the wind turbine. They explained that this phenomenon is due to the blade-tip vortex interactions that are stronger in the region of upcoming blades than in the region of retreating ones. They also showed that the wake deflection is reduced gradually at very high tip-speed ratios, at which the flow recognises the turbine rotor as a porous cylinder, with symmetric deflection of the wake. More recently, Araya and Dabiri [13] used particle image velocimetry (PIV) and compared wake characteristics of a turbine whose rotation is either driven by the incoming flow or prescribed by a motor. They found that the turbine kinematics and aerodynamic properties are the only factors that govern the wake dynamics, regardless of the means to drive the turbine blades.

Besides wind tunnel experiments, some numerical studies have also been used to investigate the wakes behind VAWTs. Two main approaches have been employed in previous studies to simulate the flow field through VAWTs. In the first approach, turbine blades and, consequently, the boundary-layer flow around them are resolved. This method can provide detailed information about the performance (e.g. turbine loading) and near-wake characteristics [6,14,15]. However, a perceived disadvantage of this approach is its increased computational complexity which precludes its use to study the wake flow in the real environment. Also, the accuracy of this method is strongly affected by the numerical method and the turbulence model employed [16,17]. The second approach is based on actuator-type techniques which remove the need for resolving the boundary-layer flow around the blades. Thus, it significantly reduces the computational cost requirements compared to full-scale blade-resolving simulations. A disadvantage of this approach is that its performance is sensitive to the aerodynamic input data of the blades. Nevertheless, due to the lower computational complexity, it is the most common method to study the wake flow downwind of VAWTs. Rajagopalan and Fanucci [18] performed one of the first numerical studies, using the second approach, to determine flow-field properties and performance of a two-dimensional VAWT. To simulate the flow, they used a numerical technique based on Patankar's 'SIMPLER' algorithm [19] in which the turbine-induced forces were modelled using an actuator-swept surface method. Later, Shen et al. [20] used the Reynolds-averaged Navier–Stokes (RANS) technique to simulate the turbulent flow field behind a two-bladed VAWT. In their simulation, a two-dimensional actuator surface technique was

used to parameterise the turbine-induced forces. They compared the obtained results with experimental data and showed that the actuator surface method combined with an incompressible Navier–Stokes solver is capable of predicting the power coefficient and forces acting on the blades with good accuracy. Bachant and Wosnik [5] compared the predictions of RANS simulations coupled with a uniform actuator disk model with experimental data. They showed that the uniform actuator disk approach is not able of accurately predicting the near-wake structure of the wake which indicated the need for improved parameterisation models. Recently, Shamsoddin and Porté-Agel [3] and Hezaveh et al. [21] used large eddy simulation (LES) combined with an actuator line technique to simulate the wake downwind of a model straight-bladed VAWT. They compared the simulated wake profiles with experimental data, and showed that LES coupled with an actuator line model is capable to yield reasonable predictions of the mean and turbulence statistics in the wake region.

The present work aims at investigating the structure of the wake behind a VAWT placed in the neutrally stratified atmospheric boundary layer (ABL). In this framework, a minimum dissipation model [22,23] is used to parameterise the subfilter stress tensor and an actuator line technique is applied to compute the turbine-induced lift and drag forces. A brief introduction of the numerical framework and the computational set-up are presented in Section 2. The validation of the LES code against the available experimental data is provided in Section 3.1. The spatial distribution of the mean velocity and the self-similar properties of the wake behind a full-scale VAWT placed in the ABL are shown and discussed in Section 3.2. In Section 3.3, a simple parameterisation of VAWTs in numerical simulations with very coarse grid resolutions is proposed. Finally, a summary and conclusions are provided in Section 4.

2. Large eddy simulation framework

2.1. LES governing equations

LES resolves the turbulent structures larger than a certain size, while the contribution of the unresolved small-scale eddies is parameterised. The LES framework used in this study is based on the filtered incompressible Navier–Stokes equations and the continuity equation:

$$\partial_i \tilde{u}_i = 0, \ \ \partial_t \tilde{u}_i + \partial_j(\tilde{u}_i \tilde{u}_j) = -\partial_i \tilde{p} + \partial_j(\nu \partial_j \tilde{u}_i) - \partial_j \tau_{ij} - \frac{f_i}{\rho} - \partial_i p_\infty, \tag{1}$$

where the tilde represents spatial filtering; $\tilde{u}_i$ is instantaneous resolved velocity in the ith direction (with $i = 1, 2, 3$ corresponding to the streamwise (x), spanwise (y) and wall-normal (z) directions, respectively); t is the time; $\tilde{p}$ is the kinematic pressure; ν is the fluid kinematic viscosity; $\tau_{ij} = \widetilde{u_i u_j} - \tilde{u}_i \tilde{u}_j$ is the subfilter stress tensor; f_i is a body force representing the effect of turbine on the flow; ρ is the constant fluid density; and $\partial_i p_\infty$ is an imposed pressure gradient. Note that all the variables in this equation are known except τ_{ij} and f_i which need to be modelled as a function of the resolved field.

2.2. Anisotropic minimum dissipation model

An important class of subfilter models consists of eddy viscosity models. These models incorporate the effect of unresolved eddies by locally increasing the molecular viscosity via an eddy viscosity. In this approach, the subfilter stress tensor is parameterised as

$$\tau_{ij}^d = \tau_{ij} - \frac{1}{3}\delta_{ij}\tau_{kk} = -2\nu_e\tilde{S}_{ij}, \tag{2}$$

where $\tilde{S}_{ij} = (\partial_i\tilde{u}_j + \partial_j\tilde{u}_i)/2$ is the resolved strain rate tensor, and ν_e is the eddy viscosity. Here, we employ the recently developed anisotropic minimum dissipation (AMD) model [22,23] to calculate the local value of the eddy viscosity without any *ad hoc* tuning. The AMD model is a simple alternative to the Smagorinsky-type approaches to parameterise the subfilter stress tensor. It provides the minimum eddy dissipation required to dissipate the energy of the subfilter scales and has many desirable practical and theoretical properties. In particular, it appropriately switches off in laminar and transitional flows; it has low computational complexity, and it is consistent with the theoretic subfilter stress tensor. The AMD eddy viscosity model is given by

$$\nu_e = \frac{\max\{-(\hat{\partial}_k\tilde{u}_i)(\hat{\partial}_k\tilde{u}_j)\tilde{S}_{ij}, 0\}}{(\partial_l\tilde{u}_m)(\partial_l\tilde{u}_m)}, \tag{3}$$

where $\hat{\partial}_k = C_k\delta_k\partial_k$ is the scaled gradient operator, in which δ_k is the size of a grid cell, and C_k is a modified Poincaré constant. The modified Poincaré constant is independent of the size of the grid cell and its magnitude only depends on the accuracy of the discretisation method (i.e. order of accuracy) for each direction. In particular, the Poincaré constant is $\sqrt{1/12}$ for a spectral method [24], and is equal to $\sqrt{1/3}$ for a second-order accurate scheme [22,25]. The AMD model has been successfully applied in simulations of decaying grid turbulence, in simulations of a temporal mixing layer and turbulent channel flow [22], and in simulations of a high-Reynolds-number rough-wall boundary-layer flow [23]. More details on the formulation of the AMD model for the subfilter stress tensor can be found in [22,23].

2.3. Wind turbine parameterisation

An actuator line technique is used to model the turbine-induced forces. Through this approach, the lift and drag forces acting on the blades are parameterised using the blade element theory and are distributed over the actuator lines representing the turbine blades. Figure 1 shows a horizontal cross-section of the blades. Different velocities, angles, and forces are shown in this figure. V_{local} is the local velocity of the incident flow at the blade. Ω is the turbine angular velocity, and R is the radius of the rotor. V_{rel} is the local velocity relative to the rotating blade, and α is the angle of attack. The turbine-induced force per unit vertical length of the blade is given by

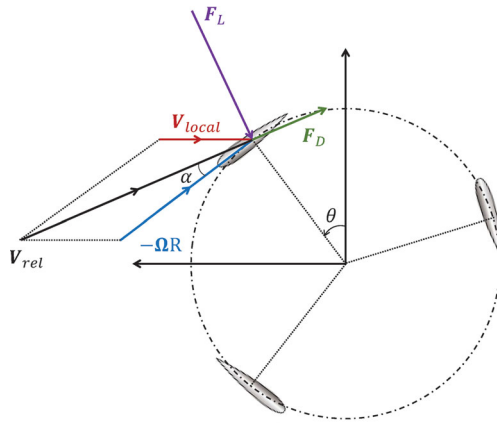$$\mathbf{f} = \frac{1}{2}\rho V_{\text{rel}}^2 c(C_L\mathbf{e}_L + C_d\mathbf{e}_D), \tag{4}$$

Figure 1. Schematic of a horizontal cross-section of VAWT blades.

where $C_L = C_L(\alpha, Re_c)$ and $C_D = C_D(\alpha, Re_c)$ are the lift and drag coefficients, respectively; Re_c is the Reynolds number based on relative velocity and chord length c; $\mathbf{e}_L$ and $\mathbf{e}_D$ denote the unit vectors in the directions of lift and drag forces, respectively. To account for the dynamic stall effect on C_L and C_D values, the modified MIT dynamic stall model [26] is employed. This method has been successfully applied in the simulation of VAWTs [3,27]. The end effects correction, similar to the one proposed by Glauert [28], is also included in the blade element analysis [29]. During the simulation, the local velocity V_{local} at the blades is known. Hence, the local velocity relative to the rotating blades V_{rel} and the angle of attack α can be obtained. Then, the resulting forces are computed using Equation (4). Noted that the applied blade forces are distributed smoothly to avoid numerical instability [30].

2.4. Numerical setup

Equation (1) is solved numerically by discretising the computational domain into N_x, N_y, and N_z uniformly spaced grid points with the resolution of $\Delta_x \times \Delta_y \times \Delta_z$ in the streamwise, spanwise, and wall-normal directions, respectively. In horizontal directions, pseudo-spectral discretisation is used, whereas the wall-normal direction is discretised with a second-order accurate method. Hence, in the AMD model, we adopt $C_x = C_y = 1/\sqrt{12}$ and $C_z = 1/\sqrt{3}$ for the modified Poincaré constant. The nonlinear terms are dealiased in Fourier space using the 3/2 rule [31]. Time integration is based on a second-order-accurate Adams–Bashforth scheme. Periodic boundary conditions are applied in the horizontal direction. To avoid the downstream wake flow affecting the inflow of the turbine due to the periodic boundary conditions, a fringe region upstream of the turbine is used to adjust the flow from the downstream state to an undisturbed inflow condition [32–35]. At the walls, Monin–Obukhov similarity theory is applied to compute the instantaneous surface shear stress [36,37].

3. Results

3.1. Code validation

The validation test case chosen for this study is based on the experiment of Brochier et al. [10] that consists of a 2-bladed VAWT operating in a water channel. The length of the channel is 150 cm, and the cross-section of the channel is a square with a side length of 20 cm. The blades consist of an NACA 0018 airfoil with a 2 cm chord length and 12 cm diameter. The height of each turbine blade is 20 cm. The diameter of the centre column of the turbine is 1 cm. The velocity measurements are available using LDV at the midspan of the turbine. In the experiment, the inflow is uniform with a velocity of $U_0 = 15$ cm/s and a turbulence intensity of about 3%, and the measurements are obtained for the tip-speed ratio of 3.85.

In the simulation of this case, the domain size in the streamwise, spanwise, and wall-normal directions are set to $L_x = 192$ cm, $L_y = 24$ cm, and $L_z = 20$ cm, respectively. To account for the effect of the side walls, in the y-direction, an immersed boundary technique following Tseng et al. [32] is used. The width of the side wall in which the immersed boundary method is applied is 4 cm. The simulations are carried out with two different spatial resolutions of GR1: $160 \times 32 \times 48$, and GR2: $240 \times 48 \times 72$ to assess the sensitivity of the simulation results to the grid resolution. The aerodynamic characteristics of the blades are obtained from the tabulated airfoil data provided by Kumar et al. [38] for low-Reynolds-number incoming flow. Note that the averaged Reynolds number based on relative velocity and chord length is about 1.155×10^4. The code is run for a long-enough time to guarantee that quasi-steady conditions are reached. After the flow reaches statistically steady condition, the quantities of interest are averaged over about 2-min time span.

Figure 2 displays the contours of instantaneous and time-averaged streamwise velocity in a horizontal $x - y$ plane at the turbine equator. As can be seen, the wake recovers with distance, as faster moving fluid gradually is entrained to the wake. The asymmetry of the wake, especially very close to the turbine, is also observed in this figure which is mainly related to the rotation of the turbine. In particular, the velocity deficit is stronger in the upcoming blade region. Similar behaviour has been reported in previous numerical and
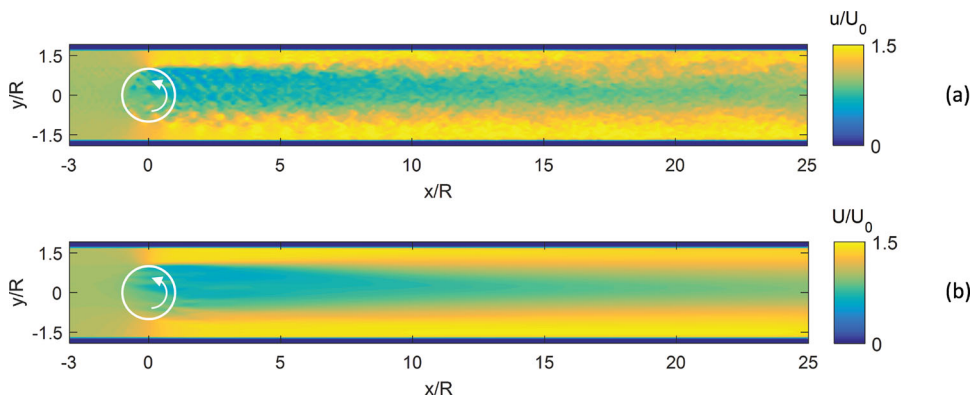

Figure 2. Contour plots of the normalised (a) instantaneous and (b) mean streamwise velocity in a horizontal plane at the equator of the turbine.
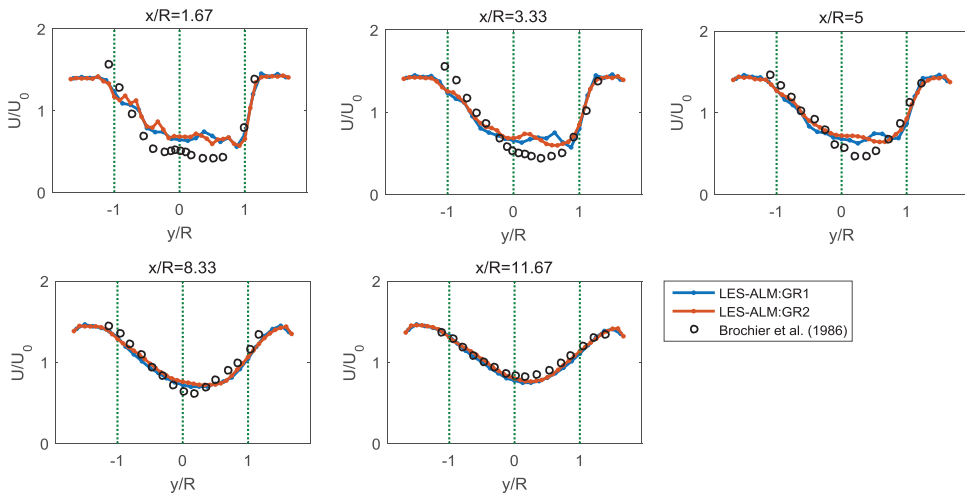
Figure 3. Comparison of lateral profiles of the normalised mean streamwise velocity obtained from two different spatial resolutions at five different downwind locations: $x/R = 1.67, 3.33, 5, 8.33,$ and 11.67.

experimental studies of the wake behind VAWTs [3,11–13,21,39–41]. It should be mentioned that, in this particular case, the wake is highly affected by the channel side walls. In particular, the blockage effect induced by the side walls leads to a substantially larger streamwise velocity in the regions between the turbine and the walls [3].

The lateral profiles of the mean streamwise velocity at the turbine equator are plotted in Figure 3, and compared with the experimental data for five different downstream locations at $x/R = 1.67, 3.33, 5, 8.33$ and 11.67. As can be seen, the pattern of the simulated mean wake is in good agreement with experimental data, especially in the far-wake region. In addition, the results show very little sensitivity to the grid resolution. Note that the observed discrepancies between the LES results and the measurement data, directly behind the turbine, are mainly related to the actuator line technique combined with the presence of the neighbouring walls. As mentioned in the introduction, in the actuator line method, the boundary-layer flow around the blades is not resolved. Hence, a larger difference between the model prediction and the experiment is anticipated in the near-wake region, where the geometrical details of the turbine greatly affect the flow structure [42]. These results demonstrate the ability of LES combined with the actuator line method to study wake structure after some downwind distance in the far wake. Since full-scale VAWTs operate in the lowest part of the ABL and, unlike the experiment considered in this section, are exposed to non-uniform and highly turbulent incoming wind, it is of great importance and beneficial to investigate the wake structure behind a full-scale VAWT sited in the ABL.

3.2. LES of the ABL flow through a full-scale VAWT

In this section, the LES framework is used to simulate the ABL turbulent flow over a stand-alone VAWT. In the simulations, the 200 kW VAWT 'T1-turbine', which is a Darrieus-type turbine with straight blades, is used. This turbine was designed and manufactured in 2010 by the company Vertical Wind AB in collaboration with Uppsala University [43]. The rotor
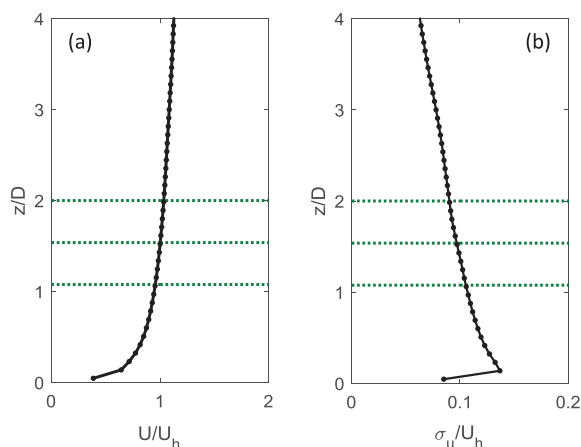
Figure 4. Vertical profiles of the (a) normalised streamwise mean velocity and (b) streamwise turbulence intensity.

consists of three long straight blades with a span (H) of 24 m. The standard NACA 0018 airfoil with a chord length of about 0.75 m was used for the blades [44]. The rotor diameter (D) is 26 m and the hub height (or equator height) of the turbine (z_h) is 40 m. Below the rated wind speed (≈ 12 m/s), the tip-speed ratio of the turbine is set to 3.8. In this study, in order to examine the effect of tip-speed ratio on the wake structure, we run the simulation for two different tip-speed ratios, $\lambda_R = 2.5$ and 3.8. The lift and drag coefficients of the blades are obtained from the tabulated airfoil data provided by Sheldahl and Klimas [45] for high-Reynolds-number incoming flow. Note that the averaged Reynolds numbers based on relative velocity and chord length are about 9.375×10^5 and 1.425×10^6 for tip-speed ratios of 2.5 and 3.8, respectively.

　　To generate the inflow conditions for the simulation of VAWT's wake, a precursor simulation of the fully developed ABL flow over a flat surface without wind turbine is performed. The domain size is discretised into $192 \times 96 \times 96$ grid points, with the resolution of $\Delta_x = 2.6$ m, $\Delta_y = 2.6$ m, and $\Delta_z = 2.4$ m. The aerodynamic surface roughness is set to 0.05 m. The boundary layer is driven by an imposed pressure gradient. The simulations are run for a long-enough time to guarantee that stationary-state conditions are achieved. After reaching statistically steady conditions, the quantities of interest are averaged over about 30-min time span. The main characteristics of the simulated ABL, including time-averaged normalised streamwise velocity and turbulence intensity, are shown in Figure 4. Note that the mean velocity at the turbine equator is about 7.5 m/s and the turbulence level is about 10%.

　　Figure 5 displays the time-averaged streamwise velocity contours in a horizontal $x - y$ plane at the equator of turbine, as well as in a vertical $x - z$ plane through the centre of the turbines, respectively, for $\lambda_R = 3.8$. The recovery and the expansion of the wake with downwind distance, in both lateral and vertical directions, is clear in this figure. The asymmetry of the wake in the top view in this figure, which is the inherent characteristic of VAWT's wakes, is also observed. This is mainly related to the greater velocity difference between the incoming flow and the upcoming blades which leads to larger turbine-induced forces and, consequently, a stronger wake in that region [40]. As can be seen, the asymmetry of the wake is stronger in the near-wake region, up to $x/D \approx 3$ in this particular case,
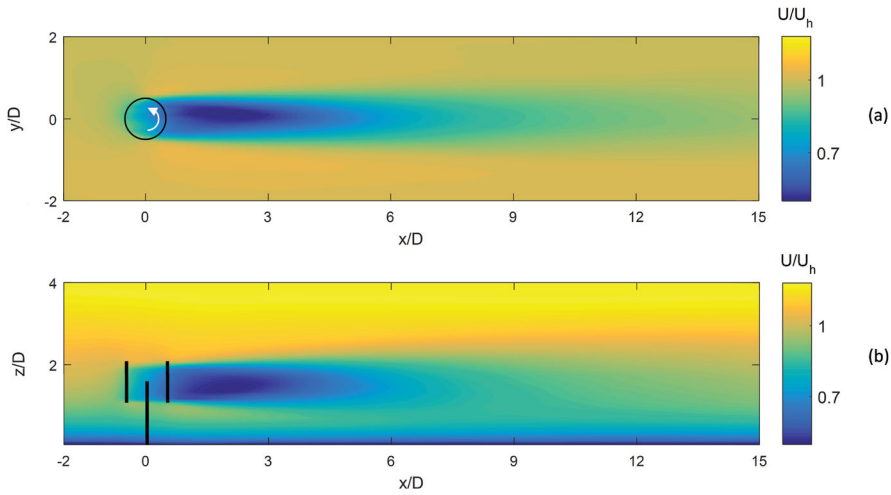
Figure 5. Contour plots of the normalised mean streamwise velocity (a) in the horizontal $x - y$ plane and (b) in the middle vertical $x - z$ plane at the centre of the turbine for $\lambda_R = 3.8$.
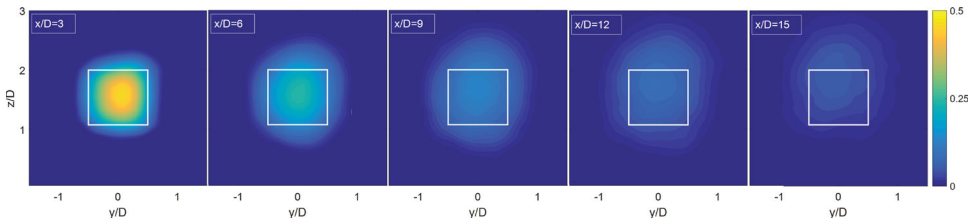

Figure 6. Contour plots of the normalised wake velocity deficit $\Delta U/U_h$ in the vertical $y - z$ plane at $x/D = 3, 6, 9, 12, 15$ downwind of the turbine for $\lambda_R = 3.8$.

and decreases as the wake is transported downstream which is consistent with the previous experimental observations [40,46].

Figure 6 shows two-dimensional fields of the normalised velocity deficit $(\Delta U/U_h)$ in the lateral cross-sectional planes at different downwind of the turbines for $\lambda_R = 3.8$, where $\Delta U = U_{in} - U$ is the mean velocity deficit, and U_{in} is the mean streamwise inflow velocity. As can be observed, the wake is recovered and also slightly shifted upward as it is transported downstream, which is mainly due to the non-uniform incoming flow induced by the presence of the ground. To have a more quantitative insight about the turbine-induced velocity deficit, the spanwise and vertical profiles of the wake velocity deficit through the centre of the turbine are also shown in Figure 7 for two different tip-speed ratios of 2.5 and 3.8. As can be seen, the wake is stronger for the higher tip-speed ratio that is attributed to the larger turbine-induced forces and, consequently, a larger effective blockage to the flow in that condition [41]. It is also observed that the asymmetry of the wake is reduced and occurs closer to the turbine by increasing the tip-speed ratio, which is consistent with the numerical experimental observations reported in [12,15,46,47]. Moreover, this figure shows that, although the incoming wind has a logarithmic profile, and the turbine has a cylindrical shape, the velocity deficit has approximately Gaussian distribution after some downwind distances for both tip-speed ratios.
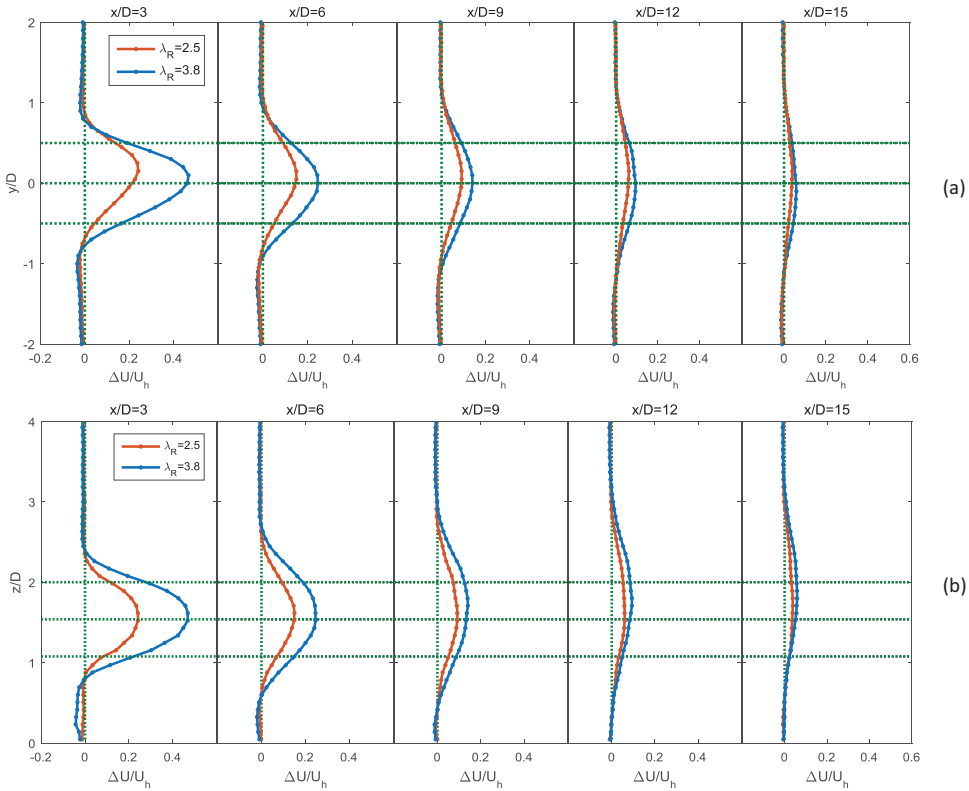
Figure 7. (a) Vertical and (b) lateral profiles of the normalised velocity deficit $\Delta U/U_h$ through the hub level at $x/D = 3, 6, 9, 12, 15$ downwind of the turbine for two different tip-speed ratios of 2.5 and 3.8.

The classical theories of shear flow (e.g. [48,49]) show that in the far-wake regions of bluff bodies in free-stream flows, the velocity deficit has a self-similar Gaussian profile. To assess the degree of self-similarity exhibited by the wake of the VAWT, we examine the scaled velocity deficit $f = \Delta U/\Delta U_{\max}$ as a function of $\eta_y = (y - y_c)/\delta_{yi}$ and $\eta_z = (z - z_c)/\delta_{zi}$, $i = 1, 2$. Here, y_c and z_c are the locations of the wake centre, and $\delta_{yi}(x)$ and $\delta_{zi}(x)$ denote the half-width of the wake in the lateral and vertical directions, respectively. The wake centre, at each downstream distance, is defined as the location where the maximum velocity deficit happens. Noted that for each lateral and vertical direction, two values for the wake's half-width are obtained corresponding to the two sides of the wake. This method allows us to account for the asymmetry of the wake as well as different lateral and vertical growth rates of the wake [50]. Figure 8 shows the self-similar velocity-deficit profiles obtained at different downwind distances in both lateral and vertical directions. In this figure, the wake's half-width $\delta_i(x)$, defined at each x as $\frac{\Delta U(r=\delta_i)}{U_{\text{hub}}} = \frac{1}{2}\frac{\Delta U_{\max}}{U_{\text{hub}}}$, is used as the characteristic wake width, where r is the radial distance from the centre of the wake. The figure shows that the profiles of $f = \Delta U/\Delta U_{\max}$ plotted against η approximately collapse into a single Gaussian curve except at the edges of the wake due to the stronger wind shear and flow acceleration at those locations [13]. The slight asymmetry observed in the scaled wake velocity-deficit profiles in the lateral direction is most likely related to the higher flow acceleration in the retreating
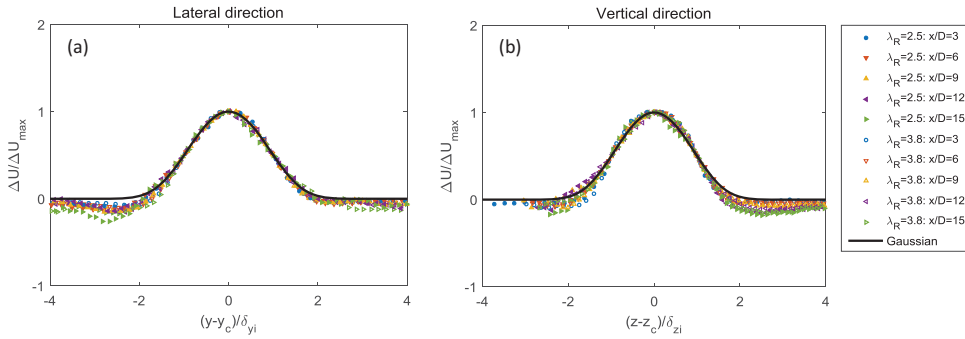
Figure 8. Scaled wake velocity-deficit profiles in the (a) lateral and (b) vertical directions, respectively, for two different tip-speed ratios of 2.5 and 3.8.

blade region compared to the upcoming blade one. This result shows that the velocity-deficit profiles can be assumed to have a self-similar shape and can be characterised by a two-dimensional multivariate Gaussian distribution after some downwind distance. These results are particularity important for developing simple wake models to predict the mean velocity-deficit downwind of the turbine.

3.2.1. Analytical wake model

Behind the wind turbine, the momentum-deficit flow rate, $\dot{M}(x)$, is defined by [49]

$$\dot{M}(x) = \int \rho U (U_{in} - U) dA. \tag{5}$$

In the self-similar region, $\dot{M}(x)$ can be re-expressed in terms of U_{in}, ΔU_{max} and $f(\eta) = \Delta U / \Delta U_{max} = \exp\left(-\frac{r^2}{2\sigma_{eq}^2}\right)$, where σ_{eq} is the equivalent standard deviation of the Gaussian-like velocity-deficit profiles at each x [51–53]. This gives

$$\dot{M} = \int \rho U_{in}^2 \left(1 - \frac{\Delta U_{max}}{U_{in}} f(\eta)\right) \left(\frac{\Delta U_{max}}{U_{in}} f(\eta)\right) dA. \tag{6}$$

Application of momentum theorem to the turbine and wake, and neglecting the viscous and pressure terms, show that the momentum-deficit flow rate $\dot{M}(x)$ is conserved and equals the total thrust (T) over the rotor area [51]:

$$\dot{M}(x) = T = \frac{1}{2} C_T \rho A_p U_{in}^2, \tag{7}$$

where C_T is the thrust coefficient computed based on the projected area of the turbine $A_p = H \times D$. By inserting Equation (7) in Equation (6) and integrating from 0 to ∞, one can obtain the following equation for the maximum velocity deficit:

$$\frac{\Delta U_{max}}{U_{in}} = 1 - \sqrt{1 - \frac{C_T}{2\pi \left(\sigma_{eq}^2 / A_p\right)}}. \tag{8}$$
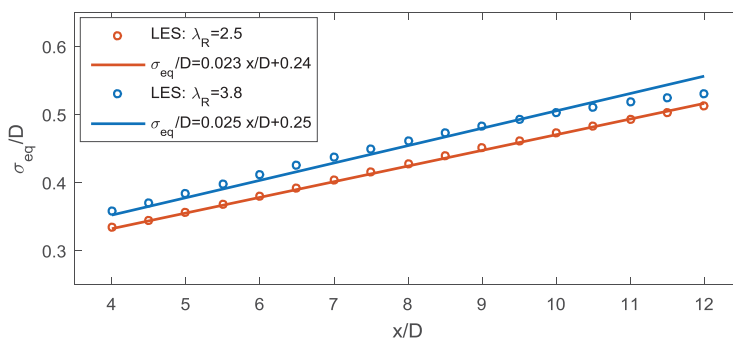
Figure 9. Normalised equivalent standard deviation of the velocity-deficit profiles for two different tip-speed ratios of 2.5 and 3.8.
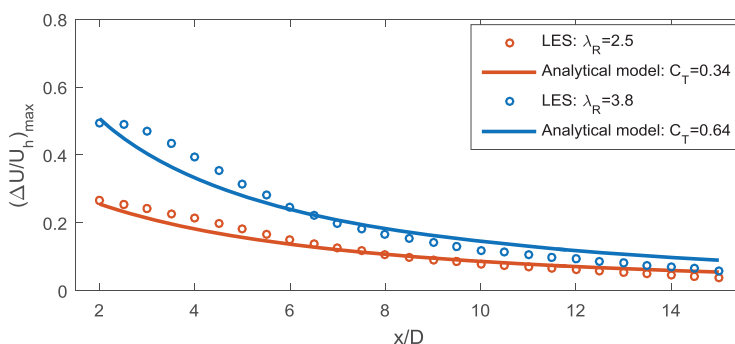

Figure 10. Comparison of the analytical model and LES data for the normalised maximum velocity deficit for two different tip-speed ratios of 2.5 and 3.8.

Note that such an approach is similar to that of Bastankhah and Porté-Agel [51] who derived an analytical wake model for HAWTs. However, unlike their model in which the wake velocity deficit is assumed to have an axisymmetric Gaussian shape, the current approach assumes that the wake velocity deficit behind a VAWT can be well characterised by a two-dimensional multivariate Gaussian distribution.

Figure 9 illustrates the variation of σ_{eq}/D as a function of normalised downwind distance. Note that the equivalent standard deviation of the wake is defined as $\sigma_{eq} = \sqrt{\sigma_y \sigma_z}$, where σ_y and σ_z are the standard deviations of the two-dimensional multivariate Gaussian distribution fitted to the velocity-deficit fields shown in Figure 6. It is found that the wake behind a VAWT expands approximately linearly in the range of $4 < x/D < 12$. It is also observed that, although the thrust coefficient (i.e. the induced forces) of the turbine is different under different tip-speed ratios, the growth rate of the wake is very similar. This finding is in agreement with the previous studies that show the wake recovery is primarily affected by the characteristics of the incoming ABL rather than the turbine loading [51,54,55].

Figure 10 shows the variation of the normalised maximum velocity deficit, as a function of normalised downwind distance, obtained from the analytical model and the LES simulation for two different tip-speed ratios. Note that, for the particular cases considered in this study, the thrust coefficient of the turbine, C_T, for the tip-speed ratios of 2.5 and 3.8 is
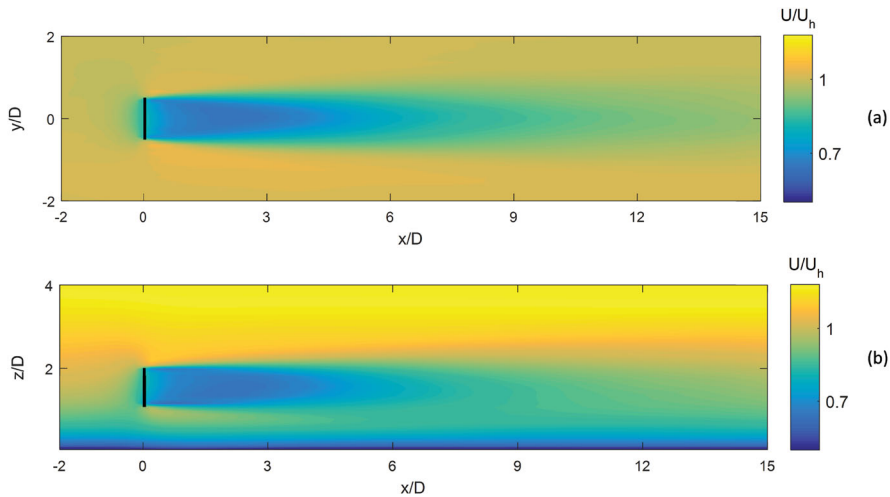
Figure 11. Contour plots of the normalised mean streamwise velocity (a) in the horizontal $x - y$ plane and (b) in the middle vertical $x - z$ plane at the centre of the rectangular porous plate.

equal to 0.34 and 0.64, respectively. As shown in this figure, the analytical model is able to predict the maximum velocity deficit in the wake downwind of the turbine reasonably well.

3.3. Parameterisation of VAWTs in LES on very coarse grid resolutions

Due to the small size and cylindrical shape of VAWTs, the simulation of VAWTs is computationally much more expensive compared to the HAWTs counterpart. Hence, in the simulation of large wind farms, including both HAWTs and VAWTs, it is of great importance to have simple parameterisation for VAWTs to reduce the computational complexity of the simulations. The most straightforward method to parameterise VAWTs in LES on very coarse grid resolutions is using a rectangular porous plate [7]. Here, we aim to compare the results obtained from the simulation of the wake behind a rectangular porous plate with the ones behind the VAWT. In the simulation of the ABL flow through the porous plate, a constant and uniform thrust coefficient is applied over the porous plate. Note that this parameterisation only considers an overall axial force, and ignores the tangential forces and the effect of the turbine-induced flow rotation. Hence, it is not able to capture the asymmetry of the wake observed in the near-wake region.

Figure 11 displays contours of the mean streamwise velocity viewed both in the horizontal direction ($x - y$ plane at turbine hub height) and the vertical direction ($x - z$ plane through the centre of the turbines). The thrust coefficient of the rectangular porous plate is set to $C_T = 0.64$ which is corresponding to the VAWT with the tip-speed ratio of 3.8. As can be seen, unlike the wake behind the VAWT, the wake is symmetric due to the uniform thrust coefficient used in this condition. In order to have more quantitative insights about the difference between the wake behind the VAWT and the porous plate, profiles of the wake velocity deficit at different downstream distances are shown in Figure 12. As shown in this figure, the difference in the velocity deficit is larger, very close to the turbine in the near-wake region (e.g. $x/D \approx 3$). This is because in the rectangular-porous-plate model,
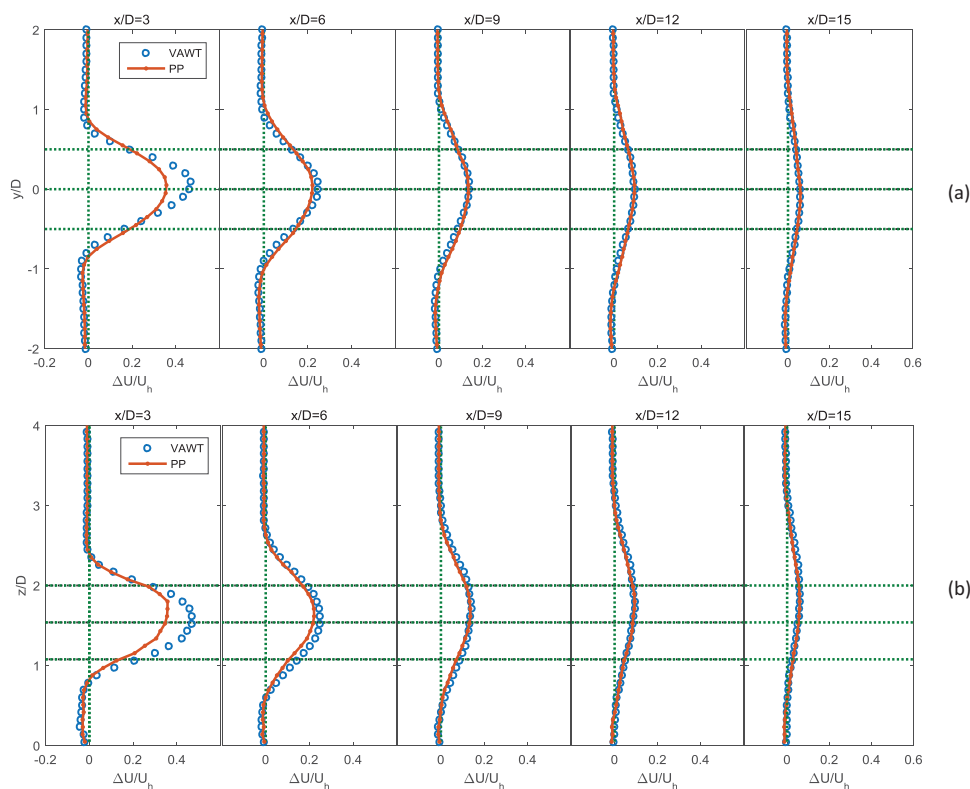
Figure 12. Comparison of the (a) vertical and (b) lateral profiles of the normalised velocity deficit $\Delta U/U_h$ through the hub level behind the VAWT for $\lambda_R = 3.8$ and behind the rectangular porous plate (PP) with $C_T = 0.64$, respectively, at $x/D = 3, 6, 9, 12, 15$.

the lateral forces as well as the non-uniform distribution of the axial force are ignored. In addition, this model is not able to resolve the tip vortices which have a significant effect on the wake, especially very close to the turbine. However, the velocity-deficit profiles are very similar after some downwind distance at $x/D \succeq 6$. This result shows that parameterisation of a VAWT as a rectangular porous plate can yield reasonable results for the mean velocity deficit at far-wake regions.

4. Summary and conclusions

In this study, LES was combined with a turbine model to investigate the structure of the wakes behind VAWTs. In the simulations, the tuning-free AMD model was used to model the subfilter stresses, and the actuator line technique was employed to parameterise the turbine-induced forces (e.g. lift and drag).

The LES framework was first validated against the laboratory data in the wake of a straight-bladed VAWT placed in the water channel. Then, it was used to study the wake behind a full-scale VAWT sited in the turbulent ABL. It was found that the wake velocity deficit has self-similar properties following a Gaussian distribution except at the edges of the turbine due to strong wind shear and flow acceleration at those regions. Inspired

by the obtained results, an analytical model was proposed and tested to predict the maximum velocity-deficit downwind of a VAWT. The proposed model is based on applying momentum theorem and assuming a two-dimensional multivariate Gaussian distribution for the wake velocity deficit. The results showed that the proposed model is able to predict the maximum velocity deficit in the wake of a stand-alone VAWT with a good accuracy.

Finally, a simple parameterisation of VAWTs for LES on very coarse grid resolutions was proposed. Through this model, the turbine is parameterised as a rectangular porous plate. A constant and uniform thrust coefficient is applied over the porous plate which is equal to the averaged thrust coefficient of the VAWT. The simulation results showed that both wind turbine models have similar predictions for the wake velocity deficit in the far-wake region. These findings are of particular importance in simulations of large wind farms including both VAWTs and HAWTs in which, due to the coarse spatial resolution, the flow around individual VAWTs is not resolved.

Disclosure statement

No potential conflict of interest was reported by the authors.

References

[1] Dabiri JO. Potential order-of-magnitude enhancement of wind farm power density via counter-rotating vertical-axis wind turbine arrays. J Renew Sustain Energy. 2011; 3: 043104.
[2] Kinzel M, Mulligan Q, Dabiri JO. Energy exchange in an array of vertical-axis wind turbines. J Turbul. 2012; 13: 1–13.
[3] Shamsoddin S, Porté-Agel F. Large eddy simulation of vertical axis wind turbine wakes. Energies. 2014; 7: 890–912.
[4] Dabiri JO, Greer JR, Koseff JR, et al. A new approach to wind energy: opportunities and challenges. AIP Conf Proc. 2015; 1652: 51–57.
[5] Bachant P, Wosnik M. Characterising the near-wake of a cross-flow turbine. J Turbul. 2015; 16: 392–410.
[6] Bremseth J, Duraisamy K. Computational analysis of vertical axis wind turbine arrays. Theor Comp Fluid Dyn. 2016:1–15.
[7] Xie S, Archer CL, Ghaisas N, et al. Benefits of collocating vertical-axis and horizontal-axis wind turbines in large wind farms. Wind Energy. 2017; 20: 45–62.
[8] Paraschivoiu I. Wind turbine design–with emphasis on Darrieus concept. Montreal: Polytechnic International Press; 2002.
[9] Araya DB, Craig AE, Kinzel M, et al. Low-order modeling of wind farm aerodynamics using leaky Rankine bodies. J Renew Sustain Energy. 2014; 6: 063118.
[10] Brochier G, Fraunie P, Beguier C, et al. Water channel experiments of dynamic stall on Darrieus wind turbine blades. AIAA J Propul Power. 1986; 2: 445–449.
[11] Bergeles G, Michos A, Athanassiadis N. Velocity vector and turbulence in the symmetry plane of a darrieus wind generator. J Wind Eng Ind Aerodyn. 1991; 37: 87–101.
[12] Battisti L, Zanne L, Dell'Anna S, et al. Aerodynamic measurements on a vertical axis wind turbine in a large scale wind tunnel. J Energy Resour Technol. 2011;133(3):031201.

[13] Araya DB, Dabiri JO. A comparison of wake measurements in motor-driven and flow-driven turbine experiments. Exp Fluids. 2015; 56: 1–15.

[14] Marsh P, Ranmuthugala D, Penesis I, et al. Three-dimensional numerical simulations of straight-bladed vertical axis tidal turbines investigating power output, torque ripple and mounting forces. Renew Energy. 2015; 83: 67–77.

[15] Posa A, Parker CM, Leftwich MC, et al. Wake structure of a single vertical axis wind turbine. Int J Heat Fluid Flow. 2016; 61: 75–84.

[16] Lam H, Peng H. Study of wake characteristics of a vertical axis wind turbine by two-and three-dimensional computational fluid dynamics simulations. Renew Energy. 2016; 90: 386–398.

[17] Chowdhury AM, Akimoto H, Hara Y. Comparative CFD analysis of vertical axis wind turbine in upright and tilted configuration. Renew Energy. 2016; 85: 327–337.

[18] Rajagopalan RG, Fanucci JB. Finite difference model for vertical-axis wind turbines. AIAA J Propul Power. 1985; 1: 432–436.

[19] Patankar S. Numerical heat transfer and fluid flow. New York (NY): McGraw Hill; 1980.

[20] Shen W, Zhang J, Sørensen J. The actuator surface model: a new Navier–Stokes based model for rotor computations. J Solar Energy Eng. 2009; 131: 011002.

[21] Hezaveh SH, Bou-Zeid E, Lohry MW, et al. Simulation and wake analysis of a single vertical axis wind turbine. Wind Energy. 2016. Available from: http://dx.doi.org/10.1002/we.2056

[22] Rozema W, Bae HJ, Moin P, et al. Minimum-dissipation models for large-eddy simulation. Phys Fluids. 2015; 27: 085107.

[23] Abkar M, Bae HJ, Moin P. Minimum dissipation scalar transport model for large-eddy simulation of turbulent flows. Phys Rev Fluids. 2016; 1: 041701.

[24] Verstappen R, Bose S, Lee J, et al. A dynamic eddy-viscosity model based on the invariants of the rate-of-strain. In: Proceedings of the Summer Program; Stanford: Center for Turbulence Research, Stanford University; 2010. p. 183–192.

[25] Verstappen R, Rozema W, Bae H. Numerical scale separation in large-eddy simulation. Proceedings of the Summer Program; Stanford: Center for Turbulence Research, Stanford University; 2014. p. 417–426.

[26] Noll RB, Ham ND. Dynamic stall of small wind systems. Burlington, MA: Aerospace Systems Inc.; 1983.

[27] Shamsoddin S, Porté-Agel F. A large-eddy simulation study of vertical axis wind turbine wakes in the atmospheric boundary layer. Energies. 2016;9(5):366.

[28] Glauert H. Airplane propellers. Aerodynamic theory. Berlin Heidelberg: Springer; 1935. p. 169–360.

[29] Bachant P, Goude A, Wosnik M. Actuator line modeling of vertical-axis turbines. arXiv preprint arXiv:1605.01449. 2016.

[30] Sørensen JN, Shen W. Numerical modeling of wind turbine wakes. J Fluids Eng. 2002; 124: 393–399.

[31] Canuto C, Hussaini M, Quarteroni A, et al. Spectral methods in fluid dynamics. Berlin: Springer; 1988.

[32] Tseng YH, Meneveau C, Parlange MB. Modeling flow around bluff bodies and predicting urban dispersion using large eddy simulation. Environ Sci Technol. 2006; 40: 2653–2662.

[33] Abkar M, Porté-Agel F. A new boundary condition for large-eddy simulation of boundary-layer flow over surface roughness transitions. J Turbul. 2012; 13: 1–18.

[34] Munters W, Meneveau C, Meyers J. Turbulent inflow precursor method with time-varying direction for large-eddy simulations and applications to wind farms. Boundary Layer Meteorol. 2015:1–24.

[35] Abkar M, Sharifi A, Porté-Agel F. Wake flow in a wind farm during a diurnal cycle. J Turbul. 2016:1–22.

[36] Moeng C. A large-eddy simulation model for the study of planetary boundary-layer turbulence. J Atmos Sci. 1984; 46: 2311–2330.

[37] Bou-Zeid E, Meneveau C, Parlange M. A scale-dependent lagrangian dynamic model for large eddy simulation of complex turbulent flows. Phys Fluids. 2005; 17: 025105.

[38] Kumar V, Paraschivoiu M, Paraschivoiu I. Low Reynolds number vertical axis wind turbine for mars. Wind Eng. 2010; 34: 461–476.

[39] Ferreira CJS, van Bussel GJ, van Kuik GA. Wind tunnel hotwire measurements, flow visualization and thrust measurement of a VAWT in skew. J Solar Energy Eng. 2006; 128: 487–497.

[40] Rolin V, Porté-Agel F. Wind-tunnel study of the wake behind a vertical axis wind turbine in a boundary layer flow using stereoscopic particle image velocimetry. J Phys Conf Ser. 2015; 625: 012012.

[41] Parker CM, Leftwich MC. The effect of tip speed ratio on a vertical axis wind turbine at high Reynolds numbers. Exp Fluids. 2016; 57: 1–11.

[42] Kang S, Yang X, Sotiropoulos F. On the onset of wake meandering for an axial flow turbine in a turbulent open channel flow. J Fluid Mech. 2014; 744: 376–403.

[43] Möllerström E, Ottermo F, Hylander J, et al. Noise emission of a 200 kW vertical axis wind turbine. Energies. 2015; 9: 19.

[44] Möllerström E. Vertical axis wind turbines: tower dynamics and noise [master's thesis]. Uppsala University; 2015.

[45] Sheldahl R, Klimas P. Aerodynamic characteristics of seven airfoil sections through 180-degree angle of attack for use in aerodynamic analysis of vertical axis wind turbines. Albuquerque (NM): Sandia National Laboratories; 1981. (Report SAND80-2114).

[46] Araya DB, Colonius T, Dabiri JO. Transition to bluff body dynamics in the wake of vertical-axis wind turbines. J Fluid Mech. Forthcoming 2016.

[47] Ryan KJ, Coletti F, Elkins CJ, et al. Three-dimensional flow field around and downstream of a subscale model rotating vertical axis wind turbine. Exp Fluids. 2016; 57: 1–15.

[48] Tennekes H, Lumley JL. A first course in turbulence. Cambridge (MA): MIT Press; 1972.

[49] Pope S. Turbulent flows. New York (NY): Cambridge University Press; 2000.

[50] Thomas FO, Liu X. An experimental investigation of symmetric and asymmetric turbulent wake development in pressure gradient. Phys Fluids. 2004; 16: 1725–1745.

[51] Bastankhah M, Porté-Agel F. A new analytical model for wind-turbine wakes. Renew Energy. 2014;70:116–123.

[52] Abkar M, Porté-Agel F. Influence of atmospheric stability on wind turbine wakes: a large-eddy simulation study. Phys Fluids. 2015; 27: 035104.

[53] Xie S, Archer C. Self-similarity and turbulence characteristics of wind turbine wakes via large-eddy simulation. Wind Energy. 2015; 18: 1815–1838.

[54] Frandsen S, Barthelmie R, Pryor S, et al. Analytical modelling of wind speed deficit in large offshore wind farms. Wind Energy. 2006; 9: 39–53.

[55] Abkar M, Porté-Agel F. Influence of the Coriolis force on the structure and evolution of wind turbine wakes. Phys Rev Fluids. 2016; 1: 063701.